J. Phys. Chem. A **2000,** *104,* 11282−11289

Model for Spectral Artifacts in Two-Dimensional Four-Wave Mixing Spectra from Absorption and Refractive Index Dispersion at Infrared Resonances

David E. Thompson[†] **and John C. Wright***

Department of Chemistry, University of Wisconsin, Madison, Wisconsin 53706

Received: June 30, 2000; In Final Form: September 18, 2000

Doubly vibrationally enhanced four-wave mixing (DOVE-FWM) is a new technique that is capable of providing two-dimensional spectra. These methods often require scanning lasers over infrared absorption features where the index of refraction dispersion and the sample absorption distort the 2D spectra. In order to test a quantitative model for treating these artifacts, we have chosen a simple model system with an isolated absorption feature and we have compared the line shapes of a resonant Raman feature for a series of different concentrations and experimental scanning strategies. We have identified the 2D spectral signatures that accompany the dispersion and absorption effects and we have shown that they are qualitatively similar to the effects introduced by singly vibrationally enhanced (SIVE) four-wave mixing. We find that the spectral changes are substantial and must be treated correctly if one is to obtain an accurate treatment of multiresonant data.

Introduction

Two-dimensional doubly vibrationally enhanced (DOVE) infrared four-wave mixing (IRFWM) spectroscopy has recently been shown to offer a number of powerful analytical capabilities for reducing spectral congestion from overlapping modes, enhancing contributions from specific components, isotopic species, or conformers in complex samples, narrowing inhomogeneously broadened lines, and providing time resolution that is determined by the vibrational dephasing times.[1−3] This method uses tunable lasers to create double vibrational coherences similar to the double spin coherences required for 2D NMR. DOVE methods are particularly well suited for studying interactions because cross peaks appear in the spectrum when the resonances are coupled by intra- or intermolecular interactions.[4,5]

DOVE methods isolate features that are associated with double vibrational coherences from other competing coherent and incoherent processes so it is now possible to perform quantitative line-shape analyses that can determine the size of the nonlinearities and model the line shapes expected from different mechanisms of system−bath coupling. The line shapes of resonances are complicated by the amplitude level interference between the background nonlinearities of the sample and the windows of our sample cell.[6]

These interferences are present whenever the overlap region of the beams encompasses both windows and sample, and arise from a phase difference in the third-order nonlinear polarizations generated in the two media. The source of this phase difference is a difference in the complex phase angles of both (1) the window and sample third-order nonlinear susceptibilities $\chi_w^{(3)}$ and $\chi_s^{(3)}$ and (2) the window and sample experimental phase matching parameters (M_w and M_s). In nonresonant IRFWM experiments the phases of the window and sample polarizations are different but constant. However, many DOVE methods require scanning infrared lasers over infrared absorption features.[7] As the frequency of a laser scans over an infrared absorption resonance, the refractive index and the absorption coefficient change continuously, modifying the amplitude and phase of the IRFWM signals generated in the sample and rear window. Because the window and sample signals naturally heterodyne, information about the changing amplitudes and phases of the sample and rear window polarizations are carried into the intensity level signal. The presence of this additional information in the DOVE line shapes, much of which arises from the linear susceptibilities (refractive index and absorption coefficient) of the window and sample, significantly complicates the spectral line shape analysis.

In order to develop and test a model for describing these artifacts, we have studied a simple system that has a well-defined Raman resonance and an isolated infrared absorption line. In this paper, we describe infrared four-wave mixing (IRFWM) scans from three different samples with increasing amounts of absorption: (1) deuteriobenzene, (2) 10% 1,8-nonadiyne:90% deuteriobenzene, and (3) 33% 1,8-nonadiyne:67% deuteriobenzene (by volume). The absorptions in these samples give rise to the possibility of a singly vibrationally enhanced (SIVE) resonant contribution to the overall four-wave mixing signal. The deuteriobenzene is used as an internal standard because the Raman resonant third-order susceptibility, $\chi^{(3)}$, of the 944 cm^{-1} ring-breathing mode is known.[8]

Two infrared beams (with frequencies ω_1 and ω_2) and a visible beam (with frequency ω_3) are focused into a sample. The intensity of the four-wave mixing signal beam generated at frequency $\omega_4 = \omega_1 - \omega_2 + \omega_3$ is monitored. In each measurement the ω_1 and ω_3 frequencies were fixed while the ω_2 frequency was scanned through the deuteriobenzene combination band at 3234 cm^{-1} (ring distorting and C−D stretching) and the 1,8 nonadiyne acetylenic C−H stretching band at 3301 cm^{-1}. By including the anomalous dispersion and the absorption explicitly in a three-layered phase-matching description, we have been able to replicate the observed line shapes. The data analysis shows that many IRFWM line-shape changes observed in scans through regions of strong absorption arise from perturbations

---

* Corresponding author. E-mail: wright@chem.wisc.edu. Fax: 608-262-0453.

[†] Present address: Department of Chemistry, Stanford University, Stanford, CA 94305-5080.

10.1021/jp002343p CCC: $19.00

of the experimental phase mismatch and changes in the window/sample interference. The line-shape changes arising from resonant FWM effects (such as SIVE or DOVE) can be masked by those arising from refractive index and absorption changes. The ability to recognize and account for the effects of absorption and anomalous dispersion in IRFWM scans provides a useful framework for cleanly isolating the resonant FWM contributions to line-shape changes in double resonance experiments.

Theory

For a three-layered sample (glass window, liquid solution, glass window) with plane parallel interfaces, Scholten et al. have described the dependence of the IRFWM signal intensity (I_4) on material properties.[6] We extend their description to three excitation beams (with intensities I_1-I_3) and we assume that the windows are transparent to all four interacting beams.

$$I_4 \propto I_1 I_2 I_3 |M_s \chi_s^{(3)} + M_w \chi_w^{(3)}|^2 \tag{1}$$

The sample and window phase-matching parameters M_s and M_w are given in eqs 2−9. The functional forms used for the third-order nonlinear susceptibilities of the sample and windows, χ_s and χ_w, are given in eqs 10−12. The explicit form of eq 1 used to fit the data is given in eq 13.

The phase matching parameters M_s and M_w depend on the window and sample wave vectors (kw_i, ks_i) and on the sample absorption coefficients (αs_i) at each experimental frequency ω_i.

$$M_s = e^{i\cdot\Delta kw\cdot lw}\left(\frac{e^{i(\Delta ks\cdot ls)}e^{-\Delta\alpha s\cdot ls} - 1}{i\Delta ks - \Delta\alpha s}\right) \tag{2}$$

$$M_w = (1 + e^{i(\Delta ks\cdot ls + \Delta kw\cdot lw)}e^{-\Delta\alpha s\cdot ls})\left(\frac{e^{i\cdot\Delta kw\cdot lw} - 1}{i\Delta kw}\right) \tag{3}$$

where ls and lw are the sample and window path lengths,

$$\Delta\alpha s = \alpha s_1 + \alpha s_2 + \alpha s_3 - \alpha s_4 \tag{4}$$

$$\Delta ks = \overline{ks_1} - \overline{ks_2} + \overline{ks_3} - \overline{ks_4} \tag{5}$$

In our experimental geometry k_1 and k_3 are collinear and k_2 is angled at θ_s. The sample phase mismatch (Δks) for this geometry is given in eq 6.

$$\Delta ks = 2\pi\{[\omega_1 ns_1 + \omega_3 ns_3]^2 + [\omega_2 ns_2]^2 + (\omega_2 ns_2)[\omega_1 ns_1 + \omega_3 ns_3]\cos(\theta s)\}^{1/2} - 2\pi\omega_4 ns_4 \tag{6}$$

An analogous expression describes the window phase mismatch, Δkw. The phase-matching angles θ_s and θ_w are calculated from the air phase-matching angle, taking into account the effects of refraction at each interface. Bertie and co-workers have measured the refractive index of neat deuteriobenzene over a wide frequency range.[9] However, the refractive index of 1,8-nonadiyne has not been reported for the frequencies of this experiment. In the absence of refractive index data for nonadiyne/deuteriobenzene mixtures, we use the Kramers−Kronig dispersion relations to express the sample refractive index as a function of the unitless absorptivity.

$$ns(\omega) = 1 + \frac{2}{\pi}P\left(\int_0^{\infty}\frac{\omega'\kappa(\omega')}{\omega'^2 - \omega^2}d\omega'\right)$$

where

$$\kappa(\omega) = \frac{2.303 A_{10}(\omega)}{4\pi\omega ls} \tag{7}$$

The pole at $\omega' = \omega$ is avoided by taking the principal value of the integral. Since our measurements of κ extend only from 2000 to 5000 cm^{-1} we rewrite eq 7 to isolate this portion of the integral.

$$ns(\omega) = 1 + \frac{2}{\pi}\left[P\int_{0\ \mathrm{cm}^{-1}}^{2000\ \mathrm{cm}^{-1}}\frac{\omega'\kappa(\omega')}{\omega'^2 - \omega^2}d\omega' + P\int_{2000\ \mathrm{cm}^{-1}}^{5000\ \mathrm{cm}^{-1}}\frac{\omega'\kappa(\omega')}{\omega'^2 - \omega^2}d\omega' + P\int_{5000\ \mathrm{cm}^{-1}}^{\infty}\frac{\omega'\kappa(\omega')}{\omega'^2 - \omega^2}d\omega'\right] \tag{8}$$

The integral from 0 to 2000 cm^{-1} represents anomalous dispersion arising from infrared and microwave transitions to the red of the ω_1 and ω_2 spectral regions. Because these have a negligible contribution to $ns(\omega)$ at the frequencies used in this experiment, this integral is assumed to be zero in our analysis. The integral from 2000 to 5000 cm^{-1} accounts for anomalous dispersion arising from infrared transitions near resonance with the ω_1 and ω_2 experimental frequencies. After obtaining $\kappa(\nu)$ from an FTIR measurement, we evaluate this integral numerically using Maclaurin's formula as recommended by Ohta and Ishida.[10] The final integral describes the electronic contribution to the refractive index that is significant at all frequencies involved in this experiment. We did not have instruments for measuring the dispersion of the electronic refractive index. Noting that deuteriobenzene and 1,8-nonadiyne have similar transparency in the visible region, and that the mixtures are predominantly deuteriobenzene, the electronic dispersion of the mixture solutions is represented as being directly proportional to that of neat deuteriobenzene. The proportionality constant is the weighted average (mol %) of the refractive indices of deuteriobenzene and 1,8-nonadiyne at 589 nm.[11]

$$\mathrm{nel}_{\mathrm{mix}}(\omega) = n_{\mathrm{deut}}(\omega)\left(\frac{\mathrm{mol}\ \%_{\mathrm{nona}} n_{\mathrm{nona589}} + \mathrm{mol}\ \%_{\mathrm{deut}} n_{\mathrm{deut589}}}{n_{\mathrm{deut589}}}\right) \tag{9}$$

Refractive index dispersion data for benzene[12] are fit to a three-coefficient dispersion equation as recommended by Bertie et al.[13] and used to estimate the refractive index for neat deuteriobenzene in the visible, $n_{\mathrm{deut}}(\omega)$. This enables evaluation of eq 8 to yield $ns(\omega)$. The refractive index nw_i of the BK7 glass windows was calculated at each experimental wavelength using the dispersion for this glass.[14]

The description of the sample's third-order susceptibility, $\chi_s^{(3)}$, includes terms for modeling the Raman resonant contribution ($\chi^{(3)}_{\mathrm{Raman}}$) from the deuteriobenzene ring mode when $\omega_1-\omega_2$ reaches resonance at 944 cm^{-1}, the nonresonant contributions ($\chi^{(3)}_{\mathrm{NRB}}$) from all sample components, and a term for the SIVE-FWM contribution ($\chi^{(3)}_{\mathrm{vib}}$) which might arise from the strong acetylenic C−H stretch at 3301 cm^{-1} in 1,8 nonadiyne. Then $\chi_s^{(3)}$ is

$$\chi_S^{(3)} = \chi^{(3)}_{\mathrm{Raman}(C_6D_6)} + \chi^{(3)}_{\mathrm{vib}(C_9H_{12})} + \chi^{(3)}_{\mathrm{NRB}} \tag{10}$$

where

$$\chi_{\mathrm{Raman}(C_6D_6)}(\omega_1,\omega_2) = \left(\frac{A_1}{\omega_{C_6D_6} - (\omega_1 - \omega_2) - i\Gamma_{C_6D_6}}\right) \tag{11}$$

$$\chi_{\text{vib}(C_9H_{12})}(\omega_1,\omega_2) = \left(\frac{A_2}{\omega_{C_9H_{12}} - \omega_2 + i\Gamma_{C_9H_{12}}}\right) \qquad (12)$$

and $\chi^{(3)}_{\text{NRB}}$ is a constant that includes the nonresonant contributions from the deuteriobenzene and 1,8 nonadiyne. The ω_{sample} and Γ_{sample} in eqs 11 and 12 are the angular frequency and dephasing rate for the C_6D_6 Raman resonance (linear frequencies of 944 and 1.4 cm^{-1}, respectively) and the C_9H_{12} vibrational resonance (linear frequencies of 3001 and 15 cm^{-1}, respectively, as measured in this work). We assume that the window susceptibility $\chi_{\text{w}}^{(3)}$ has a constant real value, A_4, and add a constant, A_5, to model baseline noise. The intensity of the four-wave mixing can then be modeled using:

$$I_4 = \left|\left(\text{MS}\left(\frac{A_1}{\omega_{C_6D_6} - (\omega_1 - \omega_2) - i\Gamma_{C_6D_6}} + \frac{A_2}{\omega_{C_9H_{12}} - \omega_2 + i\Gamma_{C_9H_{12}}} + A_3\right) + M_{\text{w}} \cdot A_4\right)\right|^2 + A_5 \qquad (13)$$

Figure 2 plots eq 13 to illustrate the nature of SIVE and phase-matching contributions to the overall I_4 line shape. The logarithmic display is chosen to accentuate the features of the baseline and in all of the plots the strong deuteriobenzene Raman feature at $(\omega_1 - \omega_2)/2\pi = 944$ cm^{-1} is prominent. Figure 2a shows the predicted spectrum if there is no absorption, refractive index dispersion, or vibrationally enhanced four-wave mixing ($A_2 = 0$ and $M_{\text{s}} = M_{\text{w}} = 1$) while Figure 2b shows the predicted spectrum with the effects of absorption and refractive index dispersion. The absorption near 3301 cm^{-1} attenuates the ω_2 beam. This absorption shortens the effective FWM path length and results in a suppression of the nonresonant background and Raman FWM mixing signals. In addition, there are line-shape changes because the sample refractive index changes rapidly in the vicinity of the absorption and alters the phase relationship between the sample and window IRFWM contributions. Plots 2c and 2d show the results of adding a SIVE feature. As can be seen in these figures, the signature of a vibrationally enhanced four wave mixing resonance ($A_2 = 0.15$, $M_{\text{s}} = 1$ and $M_{\text{w}} = 1$) is very similar to the signature of absorption/dispersion effects. This similarity makes it challenging to experimentally distinguish the two effects.

Experimentally, it is difficult to measure the absolute signal intensity in four-wave mixing experiments so in all the experiments, the deuteriobenzene Raman feature serves as internal intensity standard that normalizes intensities in spectra taken at different ω_1 or ω_2 values, depending upon which frequency is scanned. In scans of ω_2 where ω_1 is fixed, the scanned range includes an absorption feature that introduces spectral artifacts from the changing values of M. Interpretation then requires that we later compare the data with a model that includes the changing M factors in order to compare the SIVE feature with the internal standard feature. In scans of ω_1 where ω_2 is fixed, the scanned range does not include absorption features that change the spectra but each spectral scan can have different phase matching and absorption effects that depend on whether ω_2 is near or at an absorption feature. Since the absorption and refractive index do not change in a spectral scan, the individual spectra do not show the effects of scanning through an absorption feature but comparisons between spectra do. One expects that this scanning strategy results in the clearest indications of SIVE features because the absorption and phase-matching effects in a scan are nearly the same for the SIVE and deuteriobenzene Raman resonance so one can compare the relative intensities more easily. Comparison of the data obtained with each scanning strategy provides a further check on the modeling and the experimental procedures.

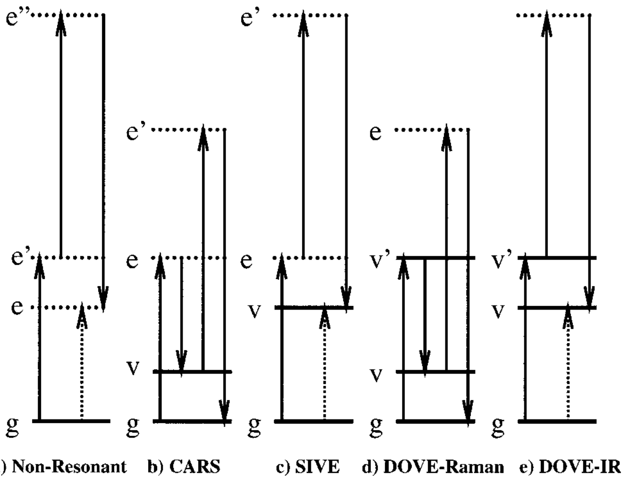

a) Non-Resonant **b) CARS** **c) SIVE** **d) DOVE-Raman** **e) DOVE-IR**

Figure 1. Wave mixing level diagrams that show the flow of coherence and resonances involved in the different processes required in this paper. The dotted arrows indicate bra side coherence changes and the dotted levels indicate virtual electronic states.

It is important to recognize that if absolute IRFWM intensities and M factors are exactly measured, both scanning strategies yield equivalent data. However, since there are experimental drifts that hinder comparisons of data taken at different times, the normalization allows one to build the 2D spectrum from 1D spectra taken at different fixed frequencies. Strategies where the frequency scans across an absorption show the effects of the changing phase-matching conditions most clearly while scans that do not include an absorption feature show a SIVE feature most clearly. Examples of these normalization strategies are illustrated in Figure 3. Figure 3a,c replot Figure 2b (with no SIVE resonance) data that is now normalized to the deuteriobenzene resonance to highlight ω_2 and ω_1 scanning strategies, respectively. Similarly in Figure 3, b and d, we replot Figure 2d (with SIVE resonance). The normalization procedure modifies the contrast and creates new contours. The effects of the SIVE resonance are apparent in the three Figures 2d and 3b,d. In Figure 2d the SIVE resonance is characterized by a difference in the IRFWM absolute intensities near $\omega_2/2\pi = 3301$ cm^{-1} and in the relative 3301 cm^{-1} intensities at different ω_1 values. In Figure 3b, the SIVE feature is seen as subtle changes in the shape and depth of the diagonal depression rising from bottom left to upper right in the spectrum. The SIVE feature in Figure 3d shows up more clearly as a dispersive peak at 3301 cm^{-1}. In all spectra, the deuteriobenzene Raman resonance is dispersive away from the absorption feature but changes in the absorption region. Although the SIVE resonance interferes with both the Raman resonance and the nonresonant terms, the changes which arise in the spectrum are subtle and do not create spectral features that are qualitatively different from those without SIVE effects.

Experimental Section

Three different sample solutions were examined in these experiments: neat deuteriobenzene, a 10% nonadiyne/90% deuteriobenzene mixture, and a 33% nonadiyne/66% deuteriobenzene mixture. These sample solutions were sandwiched between two 100 μm thick glass windows in a variable path length cell. The sample and window path length (l_{s} and l_{w}) are calculated from a measured infrared absorbance.

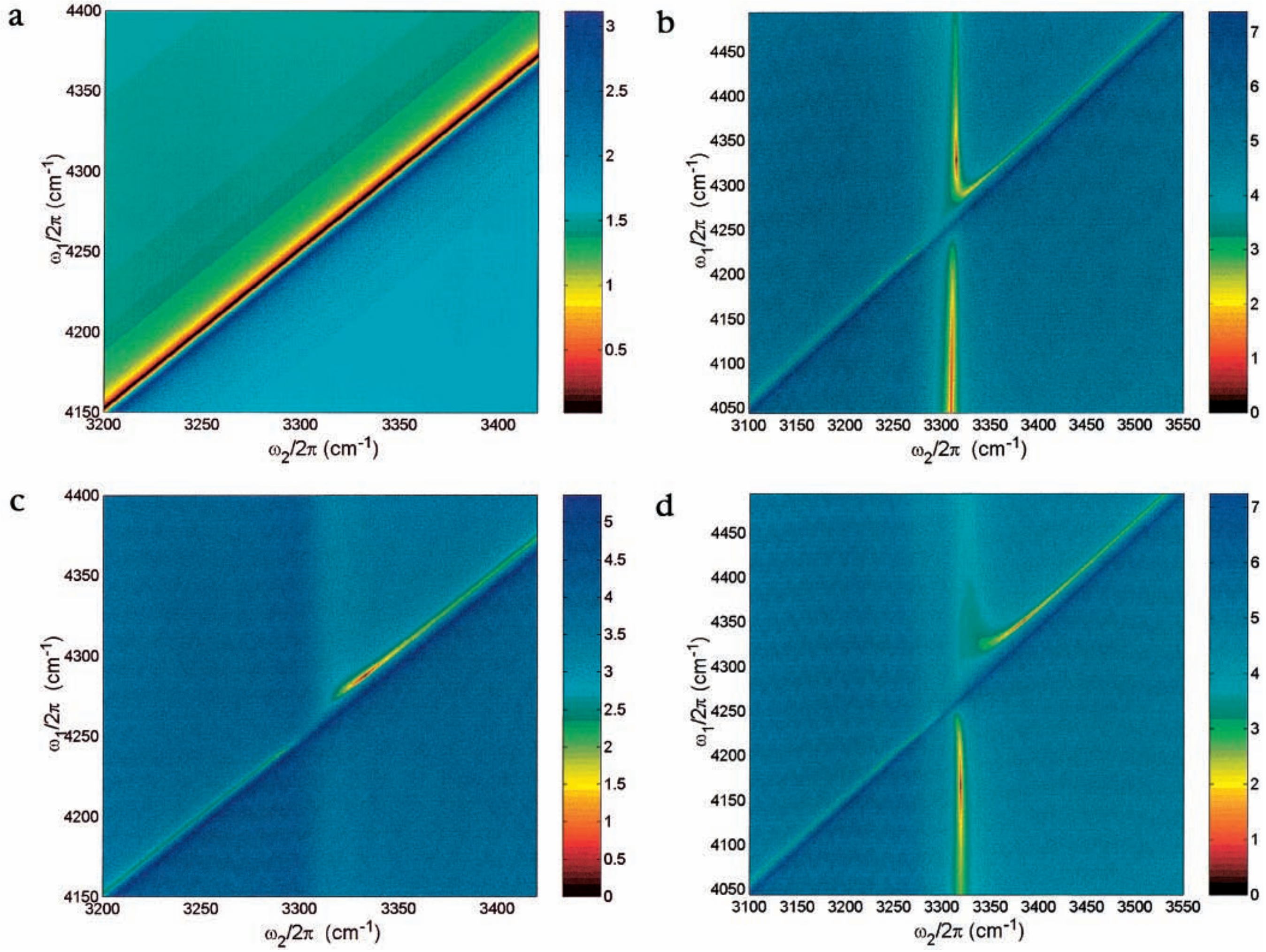

Figure 2. Simulations of spectra with and without absorption and refractive index effects and with and without a SIVE resonance. (a) No SIVE, absorption, or refractive index effects, $M_s = M_w = 1$, $A_2 = 0$. (b) No SIVE but absorption and refractive index effects are included, $A_2 = 0$. (c) SIVE but no absorption or refractive index effects, $A_2 = 0.15$, $M_s = M_w = 1$. (d) SIVE, absorption, and refractive index effects are included, $A_2 = 0.15$. The *z*-axis shows the logarithm of the four wave mixing intensity.

The sample is placed at the intersection of three focused beams, designated by their frequencies ω_1, ω_2, and ω_3. The ω_1 and ω_2 beams are each created via difference frequency generation between a dye laser and the 1.06 μm YAG fundamental in a $LiNbO_3$ crystal. The ω_3 beam is generated by frequency doubling the YAG fundamental. The intensities of the ω_1 and ω_2 beams are measured and used to correct the signal intensity for fluctuations. The paths of the ω_1 and ω_3 beams are combined just prior to the sample ensuring that both beams enter the sample collinearly and at normal incidence. The ω_2 beam crosses the other two beams at a 14.6° angle (measured in air). The overlap region of the three beams extends over the full length (~300 μm) of the sample sandwich and generates a material polarization which launches the IRFWM beam with frequency $\omega_4 = \omega_1 - \omega_2 + \omega_3$. The IRFWM signal beam exits the sample at an angle of 2.5° with respect to the ω_1 and ω_3 beams and 17° with respect to the ω_2 beam. After traveling ~1 m (to allow good spatial separation from the input beams), passing through two spectral filters (to reduce scattered light at low signal levels), the IRFWM signal is detected with a photomultiplier tube. In the neat deuteriobenzene and 10% 1,8-nonadiyne experiments, the sensitivity in weak signal portions of the scan was considerably improved by attenuating the IRFWM signal (with optical density) only where resonant peaks would have otherwise saturated the detector.

In each spectrum, the ω_2 frequency is scanned over two vibrational absorption features (the ring distorting and C−D stretching combination band in deuteriobenzene at 3234 cm^{-1} and the acetylenic C−H stretch in nonadiyne at 3301 cm^{-1}) while the frequencies of the ω_1 and ω_3 beams are held fixed. The ω_1 frequency is selected so that the Raman transition at $\omega_1 - \omega_2$ (the ring breathing mode of deuteriobenzene at 944 cm^{-1}) is prominent in each scan, and is systematically stepped between scans so that the relative position of the vibrational and Raman features walk across one another over the series of scans comprising the experiment. Finally, we note that there are three other much weaker Raman lines in this vicinity. The strongest of these is the deuteriobenzene Raman line at 868 cm^{-1}. Although we did not fit this line, it is present in the neat deuteriobenzene and the 10% nonadiyne data. On the other hand, the 1,8-nonadiyne Raman lines at 931 and 936 cm^{-1}, respectively, are not observed, most likely due to masking by the much stronger deuteriobenzene 944 cm^{-1} line.

Results

Figures 4−6 present the data obtained in the three experiments: (I) neat deuteriobenzene, (II) 10% nonadiyne/90% deuteriobenzene, (III) 33% nonadiyne/66% deuteriobenzene. Each figure is composed of scatter plots displaying the IRFWM signal collected in individual ω_2 scans, corrected for baseline

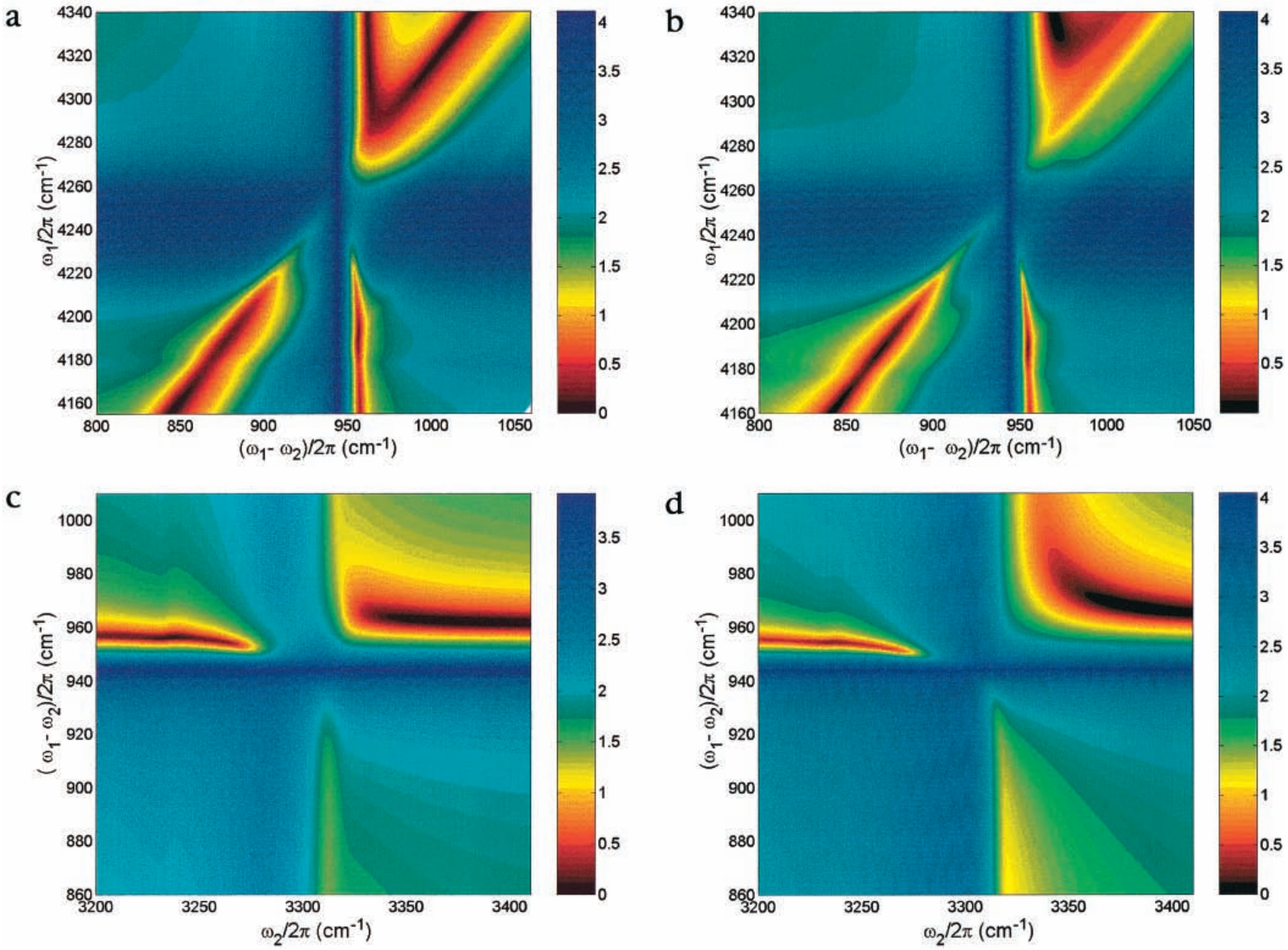

Figure 3. Simulations of experimental spectra where either ω_1 was fixed while $\omega_1 - \omega_2$ was scanned (top row) or either ω_2 was fixed while $\omega_1 - \omega_2$ was scanned (bottom row). In each case, the spectra are normalized by the deuteriobenzene Raman feature at $(\omega_1 - \omega_2)/2\pi = 944$ cm^{-1}. The left-hand spectra have no SIVE contribution ($A_2 = 0$) while the right-hand spectra have a SIVE contribution ($A_2 = 0.15$). The *z*-axis shows the logarithm of the four wave mixing intensity.

offsets and input beam intensity fluctuations. A log scale on the ordinate axes highlights the consistent and reproducible changes observed in the baseline over the course of each ω_2 scan. Nonlinear regression analysis found the best fitting parameters for fitting A_1−A_4 in eq 13. The fits are displayed as lines running through the scatter plots. Running above each spectrum is the sample absorbance over the relevant ω_2 scan range so it is clear where the absorption resonances are located.

Two primary characteristics of these IRFWM signals are (1) the "nonresonant background" IRFWM signal which is always present and observable (even far from resonant interactions) and (2) the prominent dispersive feature in the IRFWM line shape arising from resonant enhancement of IRFWM by the Raman line at 944 cm^{-1}. At the beginning of an ω_2 scan, as ω_1−ω_2 scans into the Raman-active deuteriobenzene ring breathing mode at 944 cm^{-1}, the Raman-enhanced resonant polarization interferes constructively with the nonresonant polarization and the I_4 climbs above the nonresonant background. When the ω_1−ω_2 frequency is above the ring-breathing mode the I_4 drops precipitously, corresponding to a shift in the resonant/nonresonant interference from constructive to destructive. With continued scanning the resonant contribution becomes weaker and the I_4 returns to the nonresonant background. An I_4 decrease is also observed each time the ω_2 frequency scans though an absorption feature. Since the I_4 generated at each point in the sample depends linearly on the ω_2 intensity, the ω_2 beam attenuation leads directly to a decrease in the I_4. The glass windows each contribute nonresonantly to the overall I_4. The I_4 generated in the front window remains constant throughout each scan but that in the rear window increases in regions of sample transparency and decreases in regions of opacity. This variation is one mechanism for the window-induced line-shape changes. A second mechanism arises from interferences between the IRFWM fields generated in the sample and windows. If the dispersion is constant, this interference simply results in a net displacement of the overall I_4 but if vibrational resonances cause anomalous dispersion, the phase relationships of the fields generated in the three layers change the interference and the overall I_4 line shape.

There are two absorption features in the spectra. The nonadiyne has the strong absorption feature at $\omega_2/2\pi = 3301$ cm^{-1} and deuteriobenzene has a weaker feature at $\omega_2/2\pi = 3234$ cm^{-1}. The deuteriobenzene feature can be seen as a depression in the four-wave mixing signal in Figure 4. Its position shifts for different ω_1 choices because the *x*-axis is ω_1−ω_2 but the absorption falls at constant ω_2 values. As the nonadiyne concentration is raised, the stronger $\omega_2/2\pi = 3301$ cm^{-1} feature dominates and causes substantial changes in the line shape and baseline, especially at the highest concentration.

By including the anomalous dispersion and the absorption explicitly in our fitting model, we have been able to account for the line-shape changes observed as one of the IRFWM input

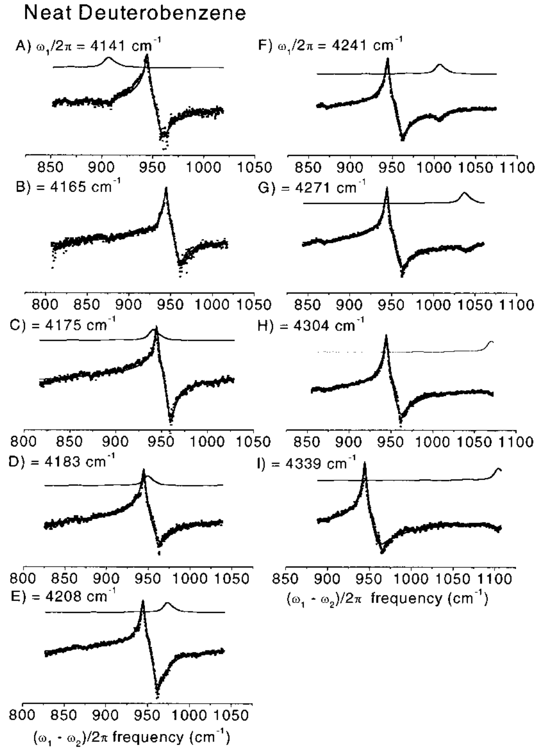

Figure 4. Experimental spectra (points) and theoretical fit (line) of a neat deuteriobenzene sample while scanning $\omega_1 - \omega_2$ for different choices of ω_1. The y-axis is logarithmic. The top spectrum in each case shows the absorption spectrum as a function of ω_2.

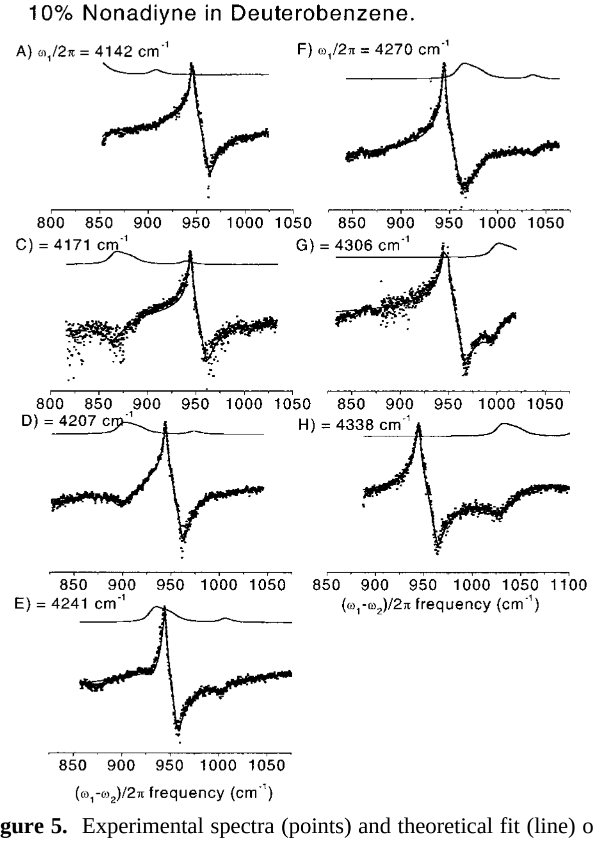

Figure 5. Experimental spectra (points) and theoretical fit (line) of a 10% 1,8-nonadiyne/90% deuteriobenzene sample while scanning $\omega_1 - \omega_2$ for different choices of ω_1. The y-axis is logarithmic. The top spectrum in each case shows the absorption spectrum as a function of ω_2.

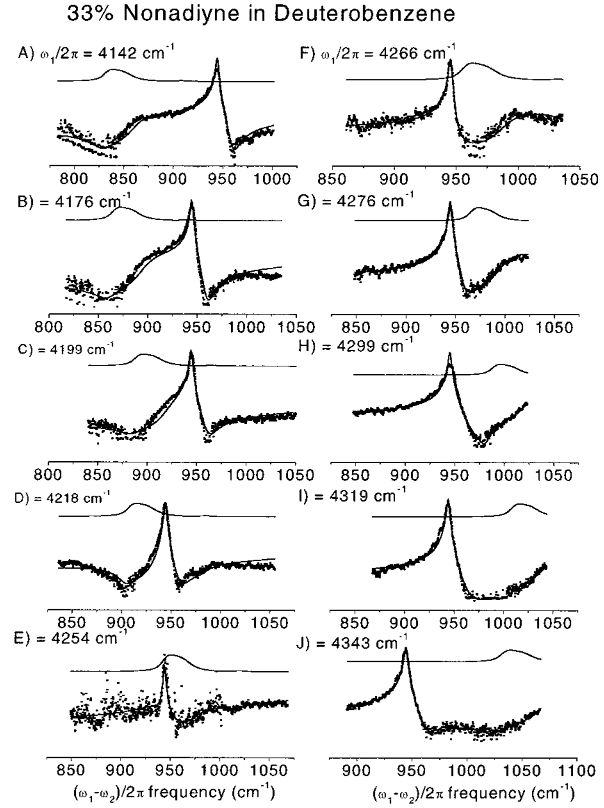

Figure 6. Experimental spectra (points) and theoretical fit (line) of a 33% 1,8-nonadiyne/67% deuteriobenzene sample while scanning $\omega_1 - \omega_2$ for different choices of ω_1. The y-axis is logarithmic. The top spectrum in each case shows the absorption spectrum as a function of ω_2.

lasers is scanned over an infrared absorption feature. The line shapes were fit to the model described earlier and the results are shown as the solid lines in Figures 4–6. The principal fitting parameters were the magnitudes of the different nonlinearities normalized relative to the deuteriobenzene 944 cm^{-1} resonance (taken as unity) and these are summarized in Table 1. Note that we did not include any contribution from the SIVE resonance. For the lower concentration nonadiyne samples, the SIVE resonance did not change the results appreciably, while for the highest concentration, good fits could be obtained with and without the SIVE resonance. This point will be discussed more fully below.

It was noted in the fitting of individual spectra that the results for each nonlinearity showed more variation when comparing the relative nonlinearities of the sample and window than comparing nonlinearities of just the sample. We attribute the differences to changes in the path length. Since the windows are only 100 μm thick, pressure changes cause bowing that changes the relative window and sample path lengths. In contrast the sample nonresonant background and the Raman peak always have an identical mixing path length. Thus, it is natural that, with the internal reference present in the *sample*, the *sample* ratios show better reproducibility than the *window* ratios.

We believe that the variations in the nonlinearity ratios in Table 1 are the result of inadequacies in the modeling and do not indicate changes of the nonlinearity within experimental error. Certainly, the nonresonant backgrounds of deuteriobenzene and nonadiyne are different so one would expect the background to change as a function of the relative concentrations. However, we do not believe the change is large enough to observe above the statistical uncertainties in the fitted parameters.

The relationships between the spectra become clearer in two-dimensional spectra. Figure 7a shows the spectral data of an

TABLE 1: Amplitudes Used for the Fitting Models[a]

	sample solution concentrations (mol%)[b]		
	$[C_6D_6] = 100\%$	$[C_6D_6] = 92.2\%$ $[C_9H_{12}] = 7.8\%$	$[C_6D_6] = 70.7\%$ $[C_9H_{12}] = 29.3\%$
$\frac{A_{\mathrm{Raman}}}{A_{\mathrm{SampleNRB}}} = \frac{A_1/\Gamma}{A_3[C_6D_6]}$	11.5 ± 0.9	9.43 ± 0.31	16 ± 3.7
$\frac{A_{\mathrm{Raman}}}{A_{\mathrm{WindowNRB}}} = \frac{A_1/\Gamma}{A_4[C_6D_6]}$	17.9 ± 3.1	13.6 ± 3.1	17.4 ± 3

[a] The resonant amplitude has been normalized by the transition line width, Γ. [b] A_2 was set = 0 in the fits which yielded these results.

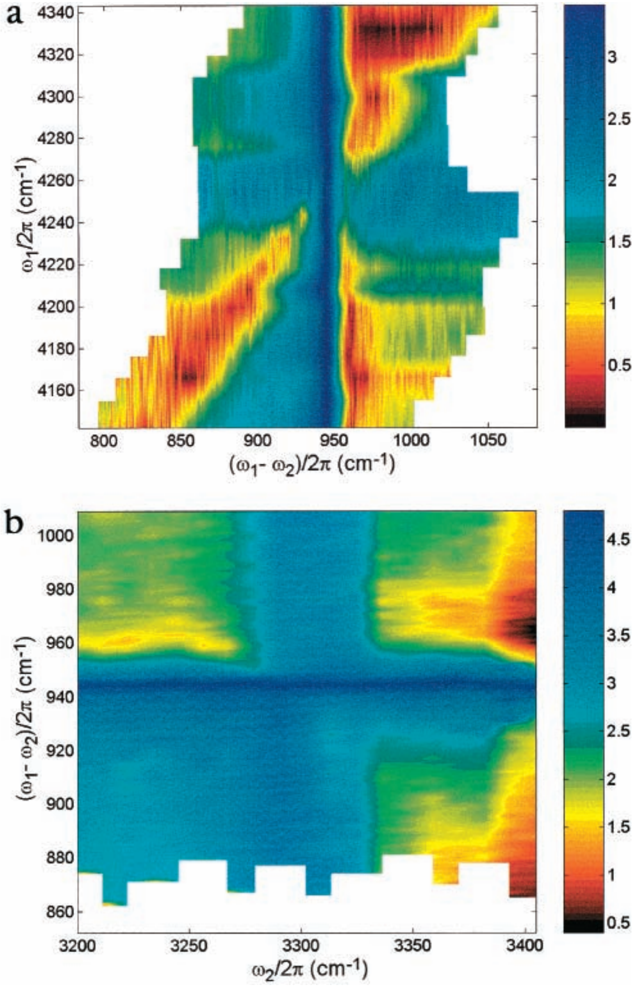

Figure 7. Two-dimensional display of the experimental data for the 33% 1,8-nonadiyne/67% deuteriobenzene sample with two different scanning and normalization strategies. (a) ω_1 was fixed while $\omega_1 - \omega_2$ was scanned. (b) ω_2 was fixed while $\omega_1 - \omega_2$ was scanned. In each case, an individual scan was normalized to the deuteriobenzene Raman resonance at $(\omega_1 - \omega_2)/2\pi = 944$ cm^{-1} and the intensity scale is logarithmic.

ω_2 scan for different ω_1 values for the highest nonadiyne concentration. The deuteriobenzene Raman line is the strongest vertical feature and the 3301 cm^{-1} absorption appears as the diagonal region of low intensity. The dispersion from the interference between the Raman line and the background is clear from the asymmetry of the low background on the right side of the line. There is a strong change in line shape when the absorption feature crosses the Raman feature because of the refractive index dispersion introduced by the absorption feature. The data are very similar to those expected from the theoretical two-dimensional spectra in Figure 3a,b. Since both simulations are so similar, it is not possible to use this data to distinguish the presence of a SIVE contribution, presumably because the absorption contributions obscure it.

Figure 7b shows the spectral data of an ω_1 scan for different ω_2 values in the same sample.[15] This scanning strategy makes the SIVE feature more prominent because the *M* factors do not change significantly in any one scan. The deuteriobenzene Raman line is the strongest horizontal feature in this figure and the 3301 cm^{-1} absorption appears as the asymmetrical vertical feature. The data are qualitatively similar to those expected from the theoretical two-dimensional spectra in Figure 3c,d. The vertical feature near 3301 cm^{-1} is stronger in the data of Figure 7b than it is in the Figure 3a simulations which do not contain the SIVE contribution but comparable to the Figure 3b simulations which do contain the SIVE contribution. This example shows that the presence of the absorption and refractive index dispersion produce features that are qualitatively similar to those in a vibrationally enhanced four-wave mixing experiment. Normalization of scans across strong absorptions results in features that obscure contributions from vibrationally resonant four-wave mixing but scans that do not include absorption features are better able to resolve vibrationally resonant four-wave mixing features.

Conclusions

It is clear that multidimensional coherent vibrational spectroscopies such as DOVE can provide capabilities for chemical measurement that are not possible with one-dimensional methods. In order to realize these capabilities, it is important to develop our ability to perform quantitative modeling of the spectra so that we can have confidence that we understand the spectroscopy. In particular, detailed line-shape analysis of the peaks and background provides an understanding of the fundamental processes that are responsible for a spectrum. Since these methods often involve the need to tune lasers into resonance with strong absorption lines, we must be confident of our ability to model the dispersion and absorption effects that control the four-wave mixing efficiency and change the line shapes. The choice of a simple system with an isolated absorption line provided an opportunity to test the quantitative capabilities of a model. It is seen that the absorption and dispersion effects mimic many of the features that are seen when vibrationally enhanced four wave mixing is present so it is important to consider these effects in interpreting multidimensional spectra. We find good agreement between the simulated two-dimensional spectra and those observed experimentally. If an experiment does not have significant contributions from windows, the model shows the relative intensity changes in a spectral scan over absorption resonances because the refractive index dispersion changes the phase matching and the absorption attenuates the excitation lasers. However, the windows of a sample cell often make significant contributions, particularly because the sample absorption shortens the effective mixing path length inside the sample so it becomes comparable to the window thickness, even if the windows are thin. In this case, the model shows there are qualitative changes in the line shape because the window contribution can add to both the real and imaginary parts of the sample nonlinearity. The complex phase angle of the phase matching factor controls the relative size of the real and imaginary parts. This phase angle depends strongly on the exact values of the refractive indices at different frequencies and the path length so accurate modeling requires accurate values for these parameters. The most definitive treatment of line shapes requires using windowless cells which eliminate the interference effects.

Acknowledgment. This work was supported by the Chemistry Program of the National Science Foundation under Grant CHE-981682

References and Notes

(1) Zhao, W.; Wright, J. C. *Phys. Rev. Lett.* **2000**, *84*, 1411−1414.
(2) Zhao, W.; Wright, J. C. *J. Am. Chem. Soc.* **1999**, *121*, 10994−10998.
(3) Zhao, W.; Wright, J. C. *Phys. Rev. Lett.* **1999**, *83*, 1950−1953.
(4) Wright, J. C.; Chen, P. C.; Hamilton, J. P.; Zilian, A.; LaBuda, M. J. *Appl. Spectrosc.* **1997**, *51*, 949−958.
(5) Cho, M.; Okumura, K.; Tanimura, Y. *J. Chem. Phys.* **1998**, *108*, 1326−1334.
(6) Scholten, T. A. H. M.; Lucassen, G. W.; Koelewijn, E.; de Mul, F. F. M.; Greve, J. *J. Raman Spectrosc.* **1989**, *20*, 503−516.
(7) Chen, P. C.; Hamilton, J. P.; Zilian, A.; LaBuda, M. J.; Wright, J. C. *Appl. Spectrosc.* **1998**, *52*, 380−392.
(8) Levenson, M. D.; Bloembergen, N. *J. Chem. Phys.* **1974**, *60*, 1323−1327.
(9) Bertie, J. E.; Lan, Z. *J. Phys. Chem. B* **1997**, *101*, 4111−4119.
(10) Ohta, K.; Ishida, N. *Appl. Spectrosc.* **1988**, *42*, 952−957.
(11) Hayman, H. J. G.; Weiss, S. *J. Chem. Phys.* **1965**, *42*, 3701−3706.
(12) Washburn, E. W., Ed. *International Critical Tables of Numerical Data Physics, Chemistry, and Technology*, 1st ed.; McGraw-Hill for National Research Council: New York, 1930; Vol. VII, p 38.
(13) Bertie, J. E.; Lan, Z. *J. Chem. Phys.* **1995**, *103*, 10152−10161.
(14) CVI. *CVI Laser Corporation Catalog*; CVI Laser Corp.: Albuquerque, NM, 1997.
(15) LaBuda, M. J.; Wright, J. C. *Chem. Phys. Lett.* **1998**, *290*, 29−35.